# Aligned fibers direct collective cell migration to engineer closing and nonclosing wound gaps

Puja Sharma[a], Colin Ng[b], Aniket Jana[b], Abinash Padhi[b], Paige Szymanski[c], Jerry S. H. Lee[d,e], Bahareh Behkam[a,b], and Amrinder S. Nain[a,b,*]

[a]School of Biomedical Engineering and Sciences and [b]Mechanical Engineering Department, Virginia Tech, Blacksburg, VA 24061; [c]Department of Bioengineering, University of Illinois at Urbana–Champaign, Urbana, IL 61801; [d]Center for Strategic Scientific Initiatives, National Cancer Institute, National Institutes of Health, Bethesda, MD 20892; [e]Chemical and Biomolecular Engineering Department, Johns Hopkins University, Baltimore, MD 21218

**ABSTRACT** **Cell emergence onto damaged or organized fibrous extracellular matrix (ECM) is a crucial precursor to collective cell migration in wound closure and cancer metastasis, respectively. However, there is a fundamental gap in our quantitative understanding of the role of local ECM size and arrangement in cell emergence–based migration and local gap closure. Here, using ECM-mimicking nanofibers bridging cell monolayers, we describe a method to recapitulate and quantitatively describe these in vivo behaviors over multispatial (single cell to cell sheets) and temporal (minutes to weeks) scales. On fiber arrays with large interfiber spacing, cells emerge (invade) either singularly by breaking cell–cell junctions analogous to release of a stretched rubber band (recoil), or in groups of few cells (chains), whereas on closely spaced fibers, multiple chains emerge collectively. Advancing cells on fibers form cell streams, which support suspended cell sheets (SCS) of various sizes and curvatures. SCS converge to form local gaps that close based on both the gap size and shape. We document that cell stream spacing of 375 μm and larger hinders SCS advancement, thus providing abilities to engineer closing and nonclosing gaps. Altogether we highlight the importance of studying cell-fiber interactions and matrix structural remodeling in fundamental and translational cell biology.**

**Monitoring Editor**
Laurent Blanchoin
CEA Grenoble

Received: May 18, 2017
Revised: Jul 14, 2017
Accepted: Jul 20, 2017

## INTRODUCTION

Small wounds gaps occurring naturally due to apoptotic release and organ remodeling are repaired efficiently through the lifetime of all multicellular organisms. However, chronic nonclosing large wounds of nonmigratory or delayed migration of the epidermis due to disease and injury adversely affect the quality of life of millions of patients across the globe (Harding *et al.*, 2002; Tsang *et al.*, 2003; Demidova-Rice *et al.*, 2012; Boulter *et al.*, 2013; Eming *et al.*, 2014; Wang *et al.*, 2016). Recently acellular extracellular (ECM) matrices have shown moderate success in allowing cells to collectively migrate upon the fibers and begin angiogenesis in chronic wounds (Lutolf and Hubbell, 2005; Frykberg and Banks, 2015). However, the contributions of fiber dimensions and layout in driving collective migration in these scaffolds and overall in the body remains unclear. Collective cell migration described as coordinated migration of multiple cells is vital to many physiological phenomena, including morphogenesis, wound healing, immune response, vascularization of tissues, and pathological conditions, including cancer metastasis (Deisboeck and Couzin, 2009; Friedl and Gilmour, 2009; Ilina and Friedl, 2009; Rørth, 2009; Aman and Piotrowski, 2010; Haeger *et al.*, 2015; Mayor and Etienne-Manneville, 2016). In vivo collective cell migration in suspended cell bridges or sheets occurs under physiological conditions involving poorly developed or absent fibrous ECM. This is well documented in *Drosophila* gastrulation, during formation of sheets by corneal epithelium and epidermis in wound healing, and also in re-epithelialization of burn wounds on areas of absent or irregular ECM (Weiss and Matoltsy, 1959; McMahon *et al.*, 2008; Oskeritzian, 2012; Vedula *et al.*, 2013, 2014). Additionally, tumors share remarkable similarities with wounds, including microenvironment remodeling, vascularization, and cell migration (Schäfer

This article was published online ahead of print in MBoC in Press (http://www.molbiolcell.org/cgi/doi/10.1091/mbc.E17-05-0305) on July 26, 2017.

Author contributions: A.S.N. designed the research. P.S., C.N., A.J., A.P., and A.S.N. performed the experiments. All authors analyzed the data. P.S., A.S.N., B.B., and J.S.H.L. wrote the manuscript.

*Address correspondence to: Amrinder S. Nain (nain@vt.edu).

Abbreviations used: AR, aspect ratio; DS, double suspended; PBS, phosphate-buffered saline; SCS, suspended cell sheets; SF, shape factor; SS, single suspended; STEP, spinneret-based tunable engineered parameters.

and Werner, 2008; Arwert *et al.*, 2012; Rybinski *et al.*, 2014). A common theme for collective cell migration in these behaviors seems to be the ability for cells to first emerge (detach from parent tissue, commonly referred to as invasion) and then migrate away from the parent tissue. Confirming this are studies reporting tip or border cells initiating migration during oogenesis, vascular sprouting, and wound closure in epithelial tissues (Gerhardt *et al.*, 2003; Somogyi and Rørth, 2004; Schmidt *et al.*, 2007; Zelenka and Arpitha, 2008; Faust *et al.*, 2011) and from edges of tumors singly or in groups (Wang *et al.*, 2002; Condeelis and Segall, 2003; Yamaguchi *et al.*, 2005; Wenger *et al.*, 2007; Ilina and Friedl, 2009; Schedin and Keely, 2011; Wirtz *et al.*, 2011; Friedl *et al.*, 2012a; Patsialou *et al.*, 2013; Weigelin *et al.*, 2014; Mayor and Etienne-Manneville, 2016).

Technologically, in vivo imaging of these behaviors and of local ECM structure has been challenging (Condeelis and Segall, 2003; Pittet and Weissleder, 2011; Webster *et al.*, 2016), and thus precise reconstruction of native fibrous environments in a controlled and repeatable manner for studying cell biology is critically needed (Friedl *et al.*, 2012b; Keely and Nain, 2015). If developed, these in vitro fibrous environments would allow scientists to engineer disease-specific models to study gastrulation, nonclosing chronic wounds, metastasis, and contributions of immune and inflammation responses after wound-inducing interventions such as radiation and surgery (Tsang *et al.*, 2003; Mustoe, 2004; Boulter *et al.*, 2013; Schaue and McBride, 2015; Wyld *et al.*, 2015; Wang *et al.*, 2016). Here we use our previously described nonelectrospinning spinneret-based tunable engineering parameters (STEP) platform (Nain and Wang, 2013; Wang and Nain, 2014) to establish an ECM-mimicking (diameter, alignment, and stiffness) in vitro assay of suspended fibers bridging cell monolayers to quantitatively link and describe emergence, collective cell migration, and wound gap closure (Figure 1). We show that interfiber spacing regulates cell emergence from the monolayer along the suspended fibers in single versus collective modes, which strikingly matches metastatic invasion modes described in vivo. Emerging cells on fibers form bundles of cells (cell streams), which resemble in vivo epithelial migratory tongues. With time, cell streams support formation and advancement of suspended cell sheets (SCS) that resemble in vivo epidermis sheets of various sizes and curvatures found during the epithelization phase in wound healing. Advancing SCS converge to form local gaps that close based on both the gap size and shape. Interestingly, we document a physical cell stream spacing of 375 µm, beyond which SCS advancement is inhibited, thus providing the ability to engineer closing and nonclosing gaps. Altogether our method provides new means to study cell–fiber interactions and matrix structural remodeling in fundamental and translational cell biology.

## RESULTS

### Interfiber separation distance regulates cell-emergence modes

Four days after a concentrated suspension of NIH3T3 fibroblasts was seeded on flat substrates interfaced with suspended nanofibers, confluent monolayers were formed. The cells from the confluent monolayers were observed to form protrusions wrapping around the suspended fibers followed by cell body alignment (polarization) along the fiber axis (Supplemental Movie M1). In time, we observed that leader cells emerged (invaded) from the monolayer onto the suspended nanofibers, (Figures 1 and 2A). We investigated the role of fiber diameters (300, 500, and 1000 nm) and interfiber spacing (0–10, 10–20, 20–30, 30–40 and 40–50 µm) on cell-emergence modes. For all tested diameters, cells exhibited three modes of emergence of leader cells: *recoil* and *chain* on single fibers and *collective* (multiple chains) on multiple fibers (Supplemental Movie M2). Recoil mode occurred primarily when the cell body was oriented at an angle with the fiber axis (Supplemental Movies M3 and M4) and after cells underwent a conditioning phase of stretching along the fiber followed by detachment through breaking of cell–cell junctions, analogous to the recoil of a stretched rubber band. The speed of detachment was found to be dependent on fiber diameter (250 ± 15, 425 ± 14, and 400 ± 30 µm/h on 300-, 500-, and 1000-nm-diameter fibers, respectively; Supplemental Figure S1). Upon detachment, the recoiling cells were observed to respread on the fiber to form elongated shapes, which would migrate either away from or toward the monolayer. Leader cells were observed to be followed by emerging follower cells. On single fibers, emergence of connected cells as cohesive chains (chain mode) was primarily observed when the cells were symmetrically distributed about the fiber axis (Supplemental Movie M5), and collective emergence was predominantly found to occur in regions of densely packed fibers with multiple chains connected with one another (Supplemental Movie M6). The mode of emergence was influenced by both fiber spacing and diameter (Figure 2B). Specifically, larger interfiber spacing favored emergence as recoils and chains, and conversely, collective emergence was observed to be the highest in densely packed fibers. Furthermore, we observed that 300- and 500-nm-diameter fibers showed a higher bias toward recoil emergence, while 1000-nm-diameter fibers showed similar probability of recoil and chain emergence, thus suggesting a role of fiber diameter and interfiber spacing in emergence dynamics.

### Kinetics of cell stream and SCS advancement in collective migration

Over time, the number of follower cells increased independent of the mode of emergence, leading to formation of cellular bundles that we termed cell streams (Figure 3A). The advancing cell streams

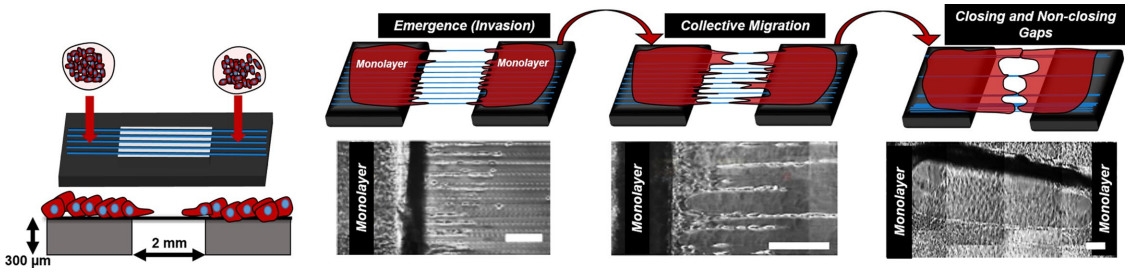


FIGURE 1: STEP-based suspended fiber platform to study cell emergence, migration, and gap closure. Schematic and phase-contrast images showing the engineered platform to study cell emergence (invasion), migration collective cell migration, and gap closure using suspended and aligned fibers interfaced with confluent monolayers. Scale bars: 200 µm.

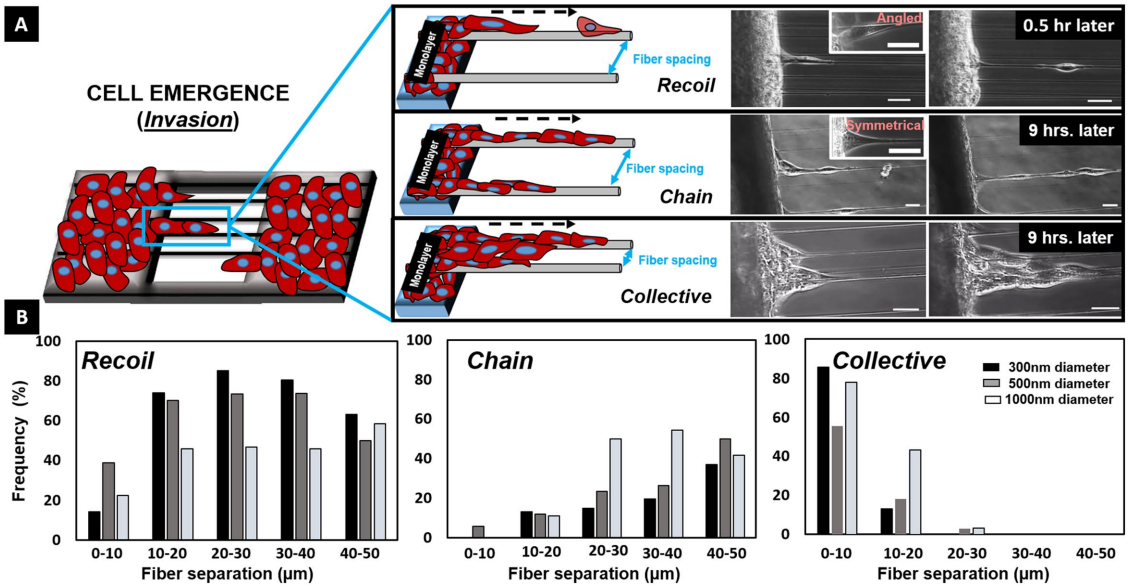


FIGURE 2: Emergence of leader cells. (A) Schematics and phase-contrast images showing leader cells leaving the monolayer in three distinct emergent modes: recoil, chain, and collective (multichain) groups. Scale bars: 25 μm. (B) Occurrence frequency of the three distinct modes of emergence on fibers of different diameters ($n$ = 124, 359, and 112 for 300-, 500-, and 1000-nm-diameter fibers respectively). Percentages have been calculated for each diameter and fiber spacing. For instance, on 300-nm-diameter fibers with <10 μm spacing, ~14% emerged as recoils, none as chains, and ~86% as multichain collective groups.

were bridged by SCS having distinct convex edges that advanced away from the monolayer (Supplemental Movie M7). To interrogate the kinetics of collective cell migration and gap closure, we tracked cell streams and SCS over days and quantitated their migratory behavior. The cell streams emerged out of the base monolayers onto suspended fibers 6 d after seeding. Within a few more days, the number of cell streams emerging out of the monolayer doubled and reached a maximum (i.e., all fibers were used for the emergence of cell streams; Figure 3B, i). Notably, cell streams initially exhibited a rapid advancement rate (~200 μm/d; Figure 3B, ii) that matched the migratory rates of highly proliferative in vivo migratory tongues typically found in early stages of wound repair (150–300 μm/d; Krawczyk, 1971; Clark *et al.*, 1982; Cavani *et al.*, 1993). We also observed the width of the individual cell streams (measured at the base, middle, and tip of streams) to increase and saturate (Figure 3B, iii). Owing to the deformability of underlying fiber networks, as the cell streams advanced away from the monolayers, they were observed to remodel the matrix and merge amongst themselves causing a reduction in number of advancing cell streams (Figure 3B, i), which increased the gap between cell streams (Figure 3C, i, and Supplemental Movie M7, shown by arrows). After 10 d, the migration rate of cell streams was observed to slow down (~20 μm/d; Figure 3B, ii), which was found to coincide with increase in SCS advancement (Figure 3C, ii). We calculated the migration rates of SCS and found them to decrease with increasing distance between adjacent cell streams (Figure 3C, iii–v). Nonlinear regression analysis showed that smaller cell stream separation distances (i.e., smaller SCS span widths) facilitated longer SCS advancement distances, and when span width exceeded 375 μm (Figure 3C, vi), shown by red arrow), SCS advancement was severely compromised. We also observed and quantitated that adjacent SCS advanced in an oscillatory manner (~70% of the time). These patterns were defined as out-of-phase, in-phase, combined, and uncoordinated. In the out-of-phase pattern, the neighboring SCS moved in opposite directions simultaneously (one toward and the other away from the monolayer), while in the in-phase mode they moved in the same direction simultaneously (toward or away from the monolayer). The combined mode was defined by the occurrence of both modes, with SCS transitioning from out-of-phase to in-phase or vice versa, and the uncoordinated mode had no observed patterns of advancement/retraction between neighboring SCS (Figure 3C, vii, and Supplemental Figure S2, i). We also quantitated the oscillatory patterns to be conserved across multiple neighboring cell sheets (Supplemental Figure S2, ii).

## Formation of gaps of various sizes and shapes and their closure dynamics

Advancing SCS from both sides of the scaffold converged and resulted in the formation of local gaps, and we investigated how gap geometry contributed to gap closure dynamics.

***Fiber architecture regulates closure time.*** To facilitate faster formation of gaps, we manufactured scaffolds in a two-layer, cross-hatch network (double suspended, DS, $N$ = 9) and compared them with our previously described single-layer, parallel (single suspended, SS, $N$ = 7) scaffolds. Interestingly, we found that the entire simulated gap spanned with DS fibers closed within 15 d, while in the same amount of time, only 30% of the gap spanned with SS fibers closed (Figure 4A and Supplemental Movies M8 and M9). While cells were observed to advance along linear tracks in parallel SS scaffolds, on cross-hatch networks of fibers, cells had more degrees of freedom to travel on multiple paths leading to faster closure (inset in Figure 4A, i). Thus, controlling fiber architecture provided us with the ability to generate gaps of various shapes and sizes on both type of fiber architectures, thus allowing us to quantitate their closure kinetics.

***Initial gap size and shape determine gap closure.*** We observed that the nucleus of cells lining the edges of all gaps were oval in

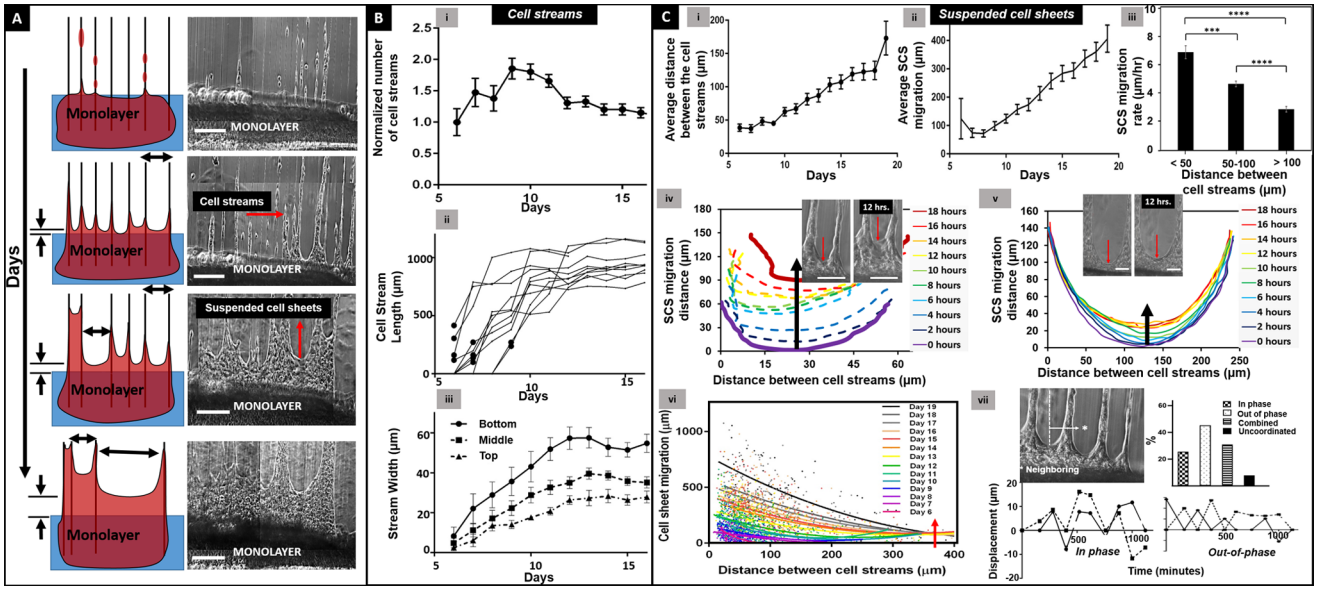


FIGURE 3: Collective migration. (A) Representative schematics and time-lapse images of cell stream and SCS advancement over time. Scale bars: 200 μm. (B) (i) Average number of cell streams normalized with respect to average number of cell streams on day 6. (ii) Kinetics of cell stream ($n$ = 10) advancement. The black dots represent the instances when the cell stream length exceeded 100 μm. (iii) Average cell stream ($n$ = 10) width measured at three locations: top, middle, and bottom of the cell streams over days. (C) (i) Increase in average distance between the cell streams (number of cell streams ($n$) = 2400). (ii) Average suspended cell sheet advancement distance over time. (iii) Decreasing SCS speed as a function of increasing cell stream separation distance ($n$ = 966). Asterisks show statistical significance. (iv, v) Examples of individual SCS front advancement-distance over time shown by black arrows in overlay of profiles for SCS separated by 60 and 250 μm, respectively. Insets are corresponding phase-contrast images showing SCS advancement over 12 h. Scale bars: 100 μm. (vi) Temporal relationship between SCS and cell stream advancement distances ($n$ = 2400). Red arrow indicates compromised SCS advancement beyond 375-μm cell stream separation distance. (vii) Representative examples of in-phase and out-of-phase displacement patterns over time of neighboring SCS. Frequency percentages of neighboring SCS advancing in-phase, out-of-phase, combined in-phase and out-of-phase, and not-coordinated modes (number of independent SCS pairs, $n$ = 64).

shape, thus suggesting them to be under mechanical tension (Supplemental Figure S3; Chancellor *et al.*, 2010; Versaevel *et al.*, 2012; Lovett *et al.*, 2013). We inquired whether this has had any effect in closure ability of gaps of varying sizes and shapes. We quantitated gap closure kinetics by using two morphodynamic metrics of area and circularity ($4\pi$ area/perimeter$^2$) to distinguish between gaps that closed and those that did not close over a period of 45 d. We identified three distinct gap size ranges that determined the ability of a gap to close (Figure 4B). The first size range (zone I) was defined by gaps of areas less than 85,000 μm$^2$. Gaps in this range adopted a variety of shapes and circularities ranging from ovals (Supplemental Movie M10) to circles (Supplemental Movie M11). However, regardless of their circularity, these gaps were able to close completely. The second size range (zone II) was defined by gaps of areas 85,000–140,000 μm$^2$. The closing of gaps in this region was dependent upon their shape, with gaps of high circularity rarely closing and oval gaps of low circularity closing completely. The third size range (zone III) was defined by gaps of areas >140,000 μm$^2$. For this size range, regardless of the circularity, gaps were unable to close in a period of at least 45 d.

***Gap shape dynamics.*** To understand the role of shapes in gap closure, we employed shape factor (SF) metric to discern gaps in zone I, and found that gaps could adopt a variety of shapes of increasing SF values: diamond (SF = 0), a perfect circle/ellipse (SF = 0.57), or a rectangle (SF = 1) (Figure 4C, ii). Frequency distribution of the SF demonstrated that the majority of the gaps adopted a SF in the ~0.65 range (circle/oval). While the SF metric was able to account for differences in majority of shapes, it could not distinguish between a circle and an ellipse. Thus, to distinguish between circular and oval gaps, we then employed the more sensitive metric of aspect ratio (AR) (Figure 4C, ii), which showed that ~60% of gaps adopted oval and elongated morphologies (AR > 1). A closer inspection (Figure 4C, iii) revealed that the AR of larger gap sizes ranged from 1 to 2.5, while those for smaller gaps occupied a wider range (1 < AR < 5) Importantly, gaps with ARs ~2.5–5 and having areas greater than ~10,000 μm$^2$ were not observed. This strongly suggests that larger gaps are less likely to occur as highly elongated ovals (AR > ~2.5).

Quantitating the temporal closure rates of gaps in zone I revealed large gaps started with an areal closure rate of 30 μm$^2$/min, and as they became smaller with time, their closure rates decreased in a nonlinear manner (Supplemental Figure S4). Additionally, we found that local gaps closed faster from regions of higher curvature (along the major axis) (Figure 4D, i). To understand this behavior, we probed the role of the acto-myosin contraction on gap closure dynamics for gaps smaller than 40,000 μm$^2$. We used previously reported dosages 10 and 20 μM of Rho kinase (ROCK) inhibitor y-27632 to compromise actin–myosin interactions (Tinevez *et al.*, 2009; Anon *et al.*, 2012; Suprynowicz *et al.*, 2012). Our results show that, under the influence of the drug, gap closure was significantly compromised for gaps in the range ~10,000–40,000 μm$^2$ (Figure 4D, ii and iii, and Supplemental Movies M12 and M13). However, gaps of smaller sizes (<~10,000 μm$^2$) exposed to y-27632 were still able to close. In fact, we found that the closure rate for gaps less than ~10,000 μm$^2$

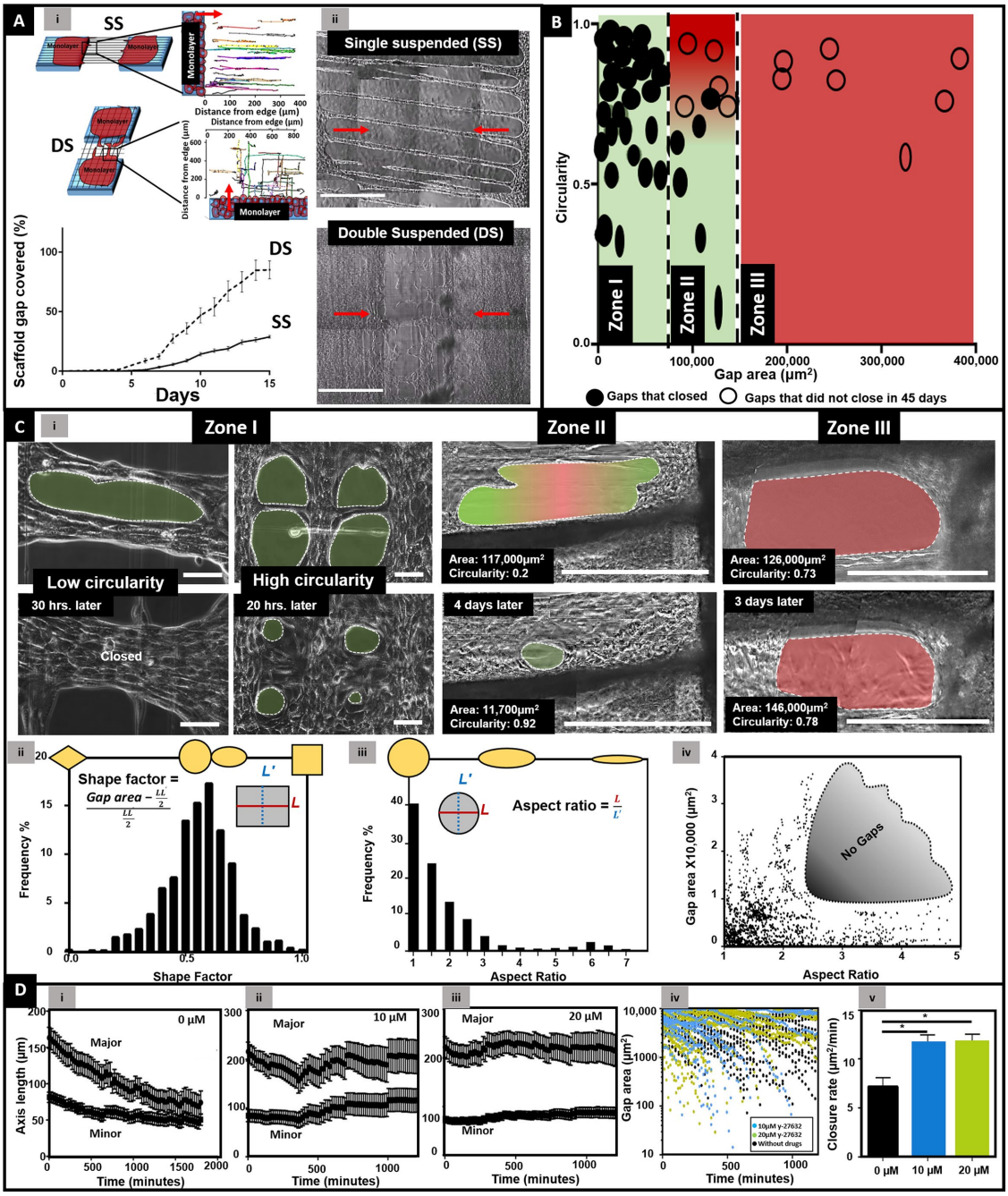


FIGURE 4: Formation and closure of gaps. (A) Schematics of SS and DS closure dynamics along with tracks of cells on respective scaffolds ($n = 25$ per category). Near-complete closure of simulated gap is achieved by cross-hatch network (DS, $N = 9$) compared with parallel networks (SS, $N = 7$). (ii) Phase-contrast images of SS and DS closure on day 12. Scale bar: 500 μm. Red arrows indicate cell migration direction from monolayer. (B) Circularity and area of gaps that closed and did not close over a period of 45 d (number of individual gaps, $n = 49$). (C) (i) Phase-contrast images of gaps that closed and did not close in the three zones. Analysis of gap shape as frequency percentage using two metrics of (ii) SF ($n = 1094$), (iii) AR ($n = 1360$) of the gaps with areas <40,000 μm$^2$, and (iv) gap area as a function of AR ($n = 819$). No gaps were observed in shaded region, suggesting large-area gaps do not form as elongated ovals (high AR). (D) (i) Changes in major and minor axes of the gaps with (i) 0 μM ($n = 25$), (ii) 10 μM ($n = 9$), and (iii) 20 μM ($n = 20$) y-27632 exposure. (iv, v) Closure of small (< 10,000 μm$^2$) gaps with y-27632 exposure (black: 0 μM; blue: 10 μM; green: 20 μM y-27632) demonstrating significantly faster closures when exposed to 10 ($n = 20$) and 20 ($n = 38$) μM y-27632 concentrations compared with those not ($n = 25$) exposed to y-27632. Asterisk shows statistical significance.

exposed to y-27632 was significantly higher than those not exposed to the drug (Figure 4D, iv and v). This result is in agreement with a study by Anon et al., which demonstrated that smaller circular gaps closed in a ROCK-independent manner (Anon *et al.*, 2012).

***Engineering closing and nonclosing gaps.*** Altogether our results demonstrate that closure of elliptical gaps is dependent on their size and shape. Our findings can be explained by deconstructing a gap into four convex SCS (Figure 5A), with each sheet having its

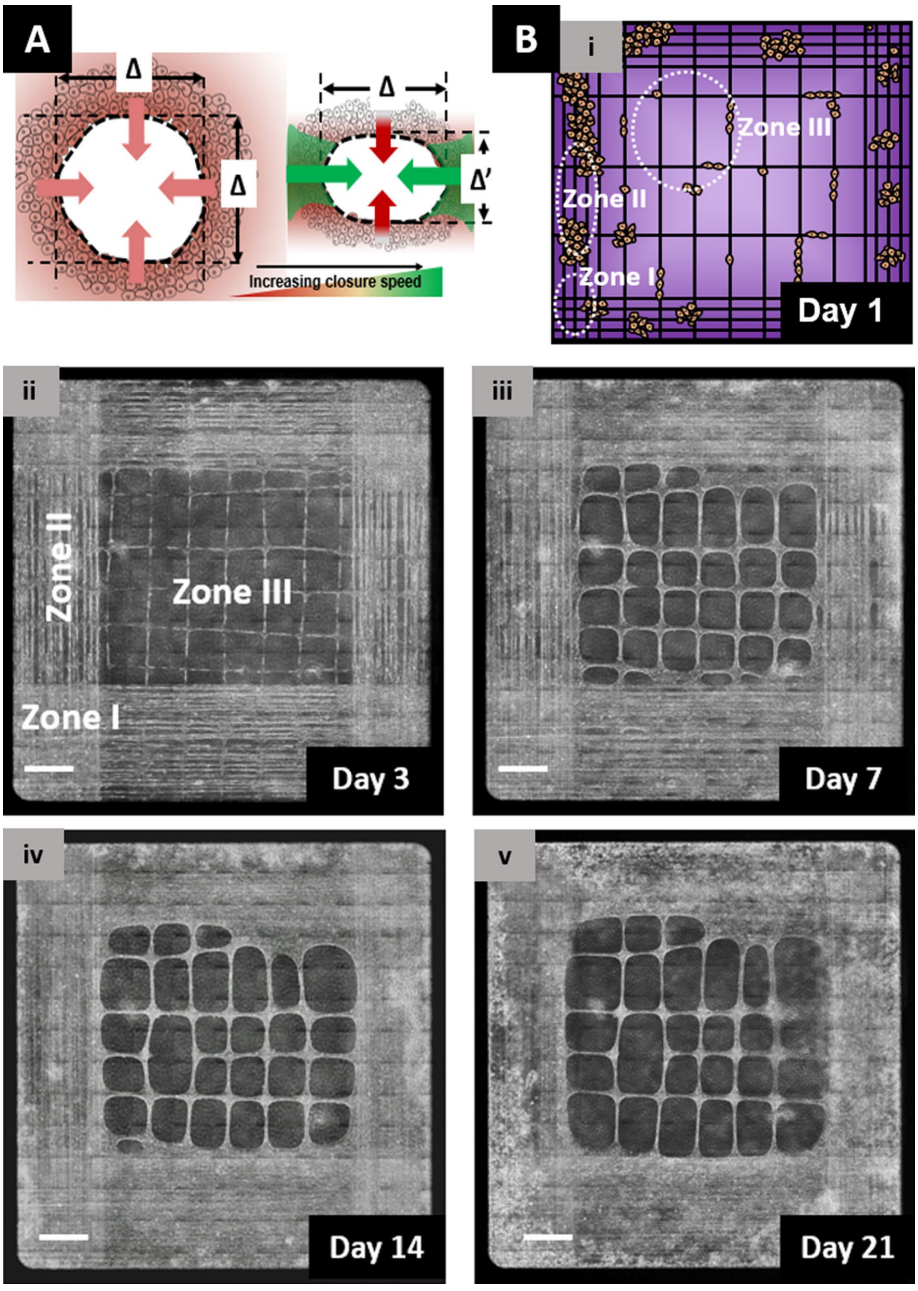


FIGURE 5: Engineering closing and nonclosing wound gaps. (A) Schematic model of closure-speed variation in response to gap shape. While circular gaps show similar closure rates from each principle direction (shown in yellow), elliptical gaps favor faster closure from high curvature (along the major axis, as shown in green) and low span distance ($\Delta' < \Delta$) direction. (B) Engineering closing and nonclosing gaps. Phase-contrast images showing closure of smaller gaps (shown by white ovals representing zones I and II, fiber spacing <50 and 100 μm, respectively) occurs in days, while gaps of large areas (zone III with spacing along horizontal axis > 375 μm) were not able to close over a 3-wk period. Scale bars: 500 μm.

corresponding width (Δ or Δ′). We know that SCS with a span width >375 μm do not advance (Figure 3C, vi); thus, if we consider the diameter of a circular gap (circularity ~1) to be 375 μm, the gap will have an area of ~110,000 μm$^2$ that falls within zone II (Figure 4B). The SCS advancement of these gaps are highly compromised, and the gaps therefore do not close. If the same gap area has a more oval shape (circularity <1), it will have SCS width less than 375 μm in one direction, which will contribute to closure of gaps (Figure 4C, i). Zone III, defined by gaps >140,000 μm$^2$, will always have SCS with span widths >375 μm, and thus, most likely will not close. To confirm this, we designed fiber networks with various interfiber spacings to achieve gaps with areas representing the three zones. Specifically, for zones I, II, and III, we deposited fibers with approximate spacing of 50, 100, and 400 μm, respectively. As expected, over a 3-wk period, we found zone I to close faster than zone II, and zone III not closing (Figure 5B and Supplemental Movie M14). Hence, by depositing fibers at precise spacing, we were able to engineer closing and nonclosing wound gaps of various sizes within the same scaffold.

## DISCUSSION

We report the development of a suspended nanofiber-based in vitro platform (Figure 1) that allows multilength-scale (single cells to collective cell sheets) investigation and quantitation of cell behavior in emergence, collective cell migration, and gap closure over multiple timescales (minutes to 45 d). Use of aligned and suspended fibers bridging monolayers provides well-defined and repeatable geometric environments to study how cells sense fiber and emerge from the monolayer, without requiring scratching of monolayers to initiate migration. In doing so, we are able to avoid the formation of irregular gaps often found in two-dimensional (2D) scratch assays, while also avoiding interference from cellular debris and biochemical factors that are released at cell death during scratching and known to affect migration (Klepeis *et al.*, 2001; Block *et al.*, 2004). We show that both fiber diameter and interfiber spacing regulate how cells emerge from the monolayers—singly or collectively—which resembles metastatic invasion reported through intravital imaging studies conducted at the tumor–matrix interface (Wang *et al.*, 2002; Condeelis and Segall, 2003; Alexander *et al.*, 2008; Friedl *et al.*, 2012a; Weigelin *et al.*, 2014). While recoiling cells had higher detachment speeds and were able to initially advance longer distances from the monolayer, they were also observed to switch directions (Supplemental Movie M15), thus having an overall lower persistence, similar to findings in the literature (Mayor and Etienne-Manneville, 2016). To achieve recoil emergence, we suggest that the cell–matrix coupling at the leading edge strengthens over time, thus providing the tensile forces necessary to overcome the cell–cell junctional forces at the rear. We believe that cells accomplish this through sensing the local ECM fiber diameter and structural stiffness; two independent parameters shown by us to be regulators of cytoskeleton arrangement, migratory behavior, and force modulation (Sharma *et al.*, 2013; Meehan and Nain, 2014; Sheets *et al.*, 2016). Postemergence, cells move out to form dense multicellular structures on fibers, and our present efforts are aimed at

understanding how cells are able to avoid one another (contact inhibition on locomotion) or come together to form multicellular clusters.

Independent of emergence mode, cells advance away from the monolayer in collective mode through formation of cell streams, which resemble and closely match the migratory rates of highly proliferative in vivo migratory tongues occurring in wound healing (0.2 mm/d on our platform compared with 0.15–0.3 mm/d shown in the literature (Krawczyk, 1971; Cavani *et al.*, 1993). Measurements of cell stream widths at the base, middle, and tip show that cell streams exist as conical structures with wider bases. We found that cell streams' migratory rate was reduced after day 10, which coincided with saturation of their widths (Figure 3B, ii and iii). Interestingly the cell stream dynamics was also observed to coincide with advancement of SCS on day 10 (Figure 3C, ii). This perhaps suggests a limit to the number of cells that can be stacked on top of each other in a cell stream, beyond which advancing or proliferating cells are directed to suspended sheets. We also observed emergence of cells from already established cell streams and SCS, which advanced cells farther away from the monolayer (Supplemental Movie M16).

A distinct and essential feature of our system is the reconfiguration of the fiber architecture due to bundling of cell streams. The reconfigurability of our fiber networks allows the formation of SCS of various widths that resemble epidermis sheets of various sizes and curvatures in vivo (Krawczyk, 1971; Clark *et al.*, 1982; Yan *et al.*, 2010). Our results showed that fiber bundling promoted widening of SCS span width, which inversely correlated with SCS advancement rates. This led us to quantitate a critical distance of 375 µm between cell streams, beyond which SCS advancement was compromised. Furthermore, the underlying relationship between cell stream separation and SCS advancement allowed us to describe dynamics of gap formation and closure to be sensitive to shapes (rectangular to diamond and including oval and circles) and sizes (small: $<10^3$ µm$^2$ to large: $>10^5$ µm$^2$). In contrast, gap closure studied using 2D scratch assays has demonstrated closure of gaps of almost all sizes and shapes (Liang *et al.*, 2007; Hulkower and Herber, 2011; Anon *et al.*, 2012). We observed that, while circular gaps closed in an isotropic manner, elliptical suspended gaps closed faster from regions of high curvature, which contrasts with 2D scratch assays, where closure is shown to occur from the direction of low curvature (Fenteany *et al.*, 2000; Jacinto *et al.*, 2001; Anon *et al.*, 2012). However, a recent interesting study using suspended cell sheets supported on rigid rectangular bridges demonstrates complete closure of gaps of smaller sizes (5–10,000 µm$^2$). Compared with our assay, these gaps fall in zone I (area < 85,000 µm$^2$), and thus, not surprisingly, close completely. Our future efforts entail interrogating the exact contributions of Rho-driven purse-string contractility and Rac-driven lamellipodial extensions (Martin and Lewis, 1992; Martin, 1997) in closure of suspended gaps of different geometries and size, as the addition of y-27632 inhibited the closure of gaps >10,000 µm$^2$ and unexpectedly closed gaps <10,000 µm$^2$ faster.

In conclusion, our multiscale platform provides new abilities to interrogate in a controlled and repeatable manner the role of fiber dimensions and layout in emergence, collective migration, and gap closure. While our platform highlights the importance of fiber properties, in future, it will require multiple layers of sophistication to include stacking of layers of fiber networks of various properties to simulate three-dimensional matrix porosity and chemical cues to recapitulate highly complex in vivo ECM structure and function. However, the current abilities of our platform provide new and exciting opportunities to generate chronic nonclosing wounds of various sizes followed by bridging them with fibers to induce gap closure, to develop scaffolds promoting migration for tissue engineering applications, and to study metastatic events in cancer biology.

## MATERIALS AND METHODS

### Scaffold preparation

Rectangular incisions were made into 300-µm-thick plastic coverslips (Fisher Scientific, Pittsburgh, PA) to create gaps of $2 \times 3$ mm$^2$. Fibers with control on diameter and spacing can be deposited by electrospinning methods (Carnell *et al.*, 2008; Liu *et al.*, 2010; Xie *et al.*, 2010). Here we used our previously reported nonelectrospinning STEP platform to deposit polystyrene fibers (Nain and Wang, 2013; Wang and Nain, 2014). Polystyrene (Scientific Polymer Products, Ontario, NY; $M_w$: $2 \times 10^6$ g mol$^{-1}$) was dissolved in p-xylene (Fisher Scientific, Pittsburgh, PA) at 8%, 10%, and 13% (wt/wt) for at least a week to prepare a polymeric solution for fiber spinning. We chose polystyrene 1) due to its high spinnability to achieve a wide range of fiber diameters that match the dimensions of ECM collagen structures (Provenzano and Vanderby, 2006; Provenzano *et al.*, 2008; Hielscher *et al.*, 2012; Kim *et al.*, 2012), and 2) because its elastic modulus (~1–3 GPa) closely matches reported values of individual collagen fibers (~2–5 GPa) (Silver *et al.*, 2003; Silver, 2006; Wenger *et al.*, 2007). Fibers were spun by extruding the solution through a hollow pipette (inside diameter ~100 µm; Jensen Global, Santa Barbara, CA). The diameters of the fibers were confirmed with scanning electron micrograph measurements. The scaffolds were tacked down in glass-bottom six-well dishes (MatTek, Ashland, MA) using high-vacuum grease (Dow Corning, Midland, MI). The scaffolds were sterilized with UV rays in a sterile biosafety cabinet (1300 Series A2; Thermo Scientific, Waltham, MA) for 20 min before cell seeding.

### Cell culture and seeding

NIH 3T3 mouse embryo fibroblasts were obtained as generous gifts from the Jarvik lab, Carnegie Mellon University, Pittsburgh, PA. As recommended by the American Type Cell Culture (ATCC), these cells were grown in T25 cell culture flasks (Corning, Corning, NY) with DMEM (HyClone, Logan, UT) and 10% bovine calf serum (ATCC, Manassas, VA). The cell culture was maintained at 37°C and 5% $CO_2$. Before the cells were seeded onto the STEP fibers, they were suspended in cell media as follows. Media from a T25 flask containing adherent NIH 3T3 fibroblasts was aspirated, and the adherent cells were rinsed with phosphate-buffered saline (PBS; Fisher Scientific, Pittsburgh, PA) twice. They were then incubated with 500 µl 0.25% trypsin (HyClone, Logan, UT) for 5 min at 37°C and suspended in fresh cell culture media. Concentrated cell suspension was seeded on two sterile plastic platforms adjacent to the suspended STEP fibers, as shown in Figure 1A, and the cells were allowed to attach overnight at 37°C and 5% $CO_2$. After cell attachment, 2 ml of cell culture media with 1% penicillin/streptomycin (HyClone, Logan, UT) was added to the well to facilitate further cell growth. The cell culture media was changed three times a week after the substrates were rinsed with PBS.

### Imaging

The scaffolds were imaged using a Zeiss microscope (Zeiss AxioObserver Z1, Jena, Germany) with incubating capacity (maintained at 37°C and 5% $CO_2$). Two distinct methods of imaging were used: 1) phase-contrast, low-magnification mosaic images of the scaffolds were obtained every day up to 2 wk after the first cells started migrating onto the suspended nanofibers, and 2) time-lapse

phase-contrast images were obtained using 20× objective to investigate cell migration and local gap closure dynamics on STEP nanofibers every 3–10 min for up to 30 h periods.

### Data analysis

The mosaic images and time-lapse movies were analyzed using Zeiss Axiovision and ImageJ software. The number of scaffolds used is denoted by *N* and individual data points by *n*.

***Cell emergence.*** Time-lapse images of cells emerging from the monolayer onto the fibers were taken. For a given fiber diameter and a given spacing, the total number of cells that emerged were calculated. Among them, the cells that emerged as recoils, chains, or multichain collective groups were identified and shown as a frequency %. Detachment speed of recoiling cells was calculated as the intranucleus distance of the emerging cell right before and after recoil divided by the time taken for recoil to occur.

***Global collective cell migration.*** For measuring the area covered by cells on the suspended nanofibers, cell cluster areas from phase-contrast images taken daily were measured using Axiovision. The summation of these cell cluster areas were then expressed as a percentage of the initial simulated gap. Cell stream separation distances were measured from the edge of one cell stream to the other using Axiovision. Similarly, the distance from the edge of the plastic platform to the closest point of the convex-shaped suspended cell sheet was measured using Axiovision and described as "suspended cell sheet (SCS) migration distance" (Figure 3C, ii).

***Local collective cell migration (local gap closure).*** Time-lapse images were used to measure local closure of suspended gaps as a function of time using Axiovision software. Gaps were observed to be typically oval in shape, and the AR of an oval gap was defined as the ratio of major to minor axis (both measured using Axiovision). For describing the shape of the corners of the gaps, we used an SF term defined as SF = (area of gap – $AB/2$)/($AB/2$), where $A$ and $B$ are the major and minor axis, respectively. Square/rectangular gap areas would have an SF of 1, circles/ovals an SF of 0.57, and a diamond shape would have an SF of 0 (Figure 4C, ii).

***Analysis of the gaps that did not close.*** Phase-contrast mosaic images of the suspended gaps were analyzed for gap closure using ImageJ software. Area and circularity measurements were made for the gaps that closed and did not close over a period of 45 d. Circularity ($4\pi$ area/perimeter$^2$) is a measure describing the shape of the gap such that a perfect circle has a circularity of 1. We performed gap area measurements for 5 consecutive days to assess the gap closure dynamics of gaps that did not close. Immunostained images of suspended gaps that did not close over a period of 45 d were also analyzed for nucleus shape using ImageJ software. The perpendicular distance from the center of the nucleus to the circumference of the gap was defined as the "distance from the edge," and the area and the circularity of the nucleus were measured as a function of its distance from the gap edge (Supplemental Figure S3). The circularity of the nucleus was measured using ImageJ software.

### Immunostaining

Substrates containing SCS of NIH 3T3s were stained for F-actin stress fibers and nucleus. Briefly, cell culture medium was aspirated out of the well plates, and the SCS were rinsed with PBS. The suspended cell sheets were fixed using a 4% paraformaldehyde in PBS solution for 15 min and were then rinsed again with PBS twice. Next, the substrates were soaked in permeabilization solution (PBS with 0.1% Triton X-100 solution) for 15 min, washed with PBS twice, and stained with Phalloidin (Santa Cruz Biotechnology, Santa Cruz, CA) at 1:80 dilution. The substrates were then stored at room temperature for 40 min, followed by PBS rinse (three times), and stained with 4′,6-diamidimo-2-phenylindole for 5 min. After the substrates were rinsed twice, they were imaged using Zeiss AxioObserver Z1.

### Drug studies

Gaps <40,000 μm$^2$ were exposed to ROCK inhibitor at 10 and 20 μM concentrations using y-27632 (Sigma Aldrich, St. Louis, MO). Its influence on local gap closure was investigated using time-lapse images taken continuously over a period of up to 30 h.

### Statistical analysis

Statistical analysis of the data was conducted using GraphPad Prism (GraphPad Software, La Jolla, CA) software. In particular, the D'Agostino and Pearson omnibus normality test was used to determine the normality of the data. When normality was verified, Analysis of variance was used to test for statistical significance, and Tukey's multiple comparison test was used to determine statistically significant differences between groups. When data were not normally distributed, a nonparametric Kruskal-Wallis test was used to test for statistical significance, and Dunn's multiple comparison test was used to determine statistical significance between groups. A $p$ value of 0.05 (*), 0.01 (**), 0.001 (***), and 0.0001 (****) was used to determine the statistical significance. Standard errors were calculated and are represented as error bars in the respective figures.


## ACKNOWLEDGMENTS

We thank Klaus Hahn (University of North Carolina) and Guy Genin (Washington University, St. Louis) for reading the article and providing critical feedback. We also thank Jon Jarvik (Carnegie Mellon University) for generously providing the NIH 3T3 cell line; AhRam Kim for her support with preliminary experiments; and Virginia Tech undergraduate volunteers Harrison Bolinger, Luke Grant, Giancarlo Di Base, Drew Smith, Ryan Grove, Liam Han, Mark Andrew Healy, and Yuxin Zheng, who helped in analyzing the data for overall gap closure (Figure 4A). We also thank James Mason Inder for help in generating Supplemental Movies 8, 9, and 14. This research was partially funded by the Bill and Andrea Waide Research Fund (Roanoke, VA), National Science Foundation (NSF) grants (CMMI-1437101 and CMMI-1462916) to A.S.N., an NSF CAREER award (CBET-1454226) to B.B., NSF REU awards (320463 and 320464), and the Institute of Critical Technology and Applied Sciences at Virginia Tech.


## REFERENCES


Alexander S, Koehl GE, Hirschberg M, Geissler EK, Friedl P (2008). Dynamic imaging of cancer growth and invasion: a modified skin-fold chamber model. Histochem Cell Biol 130, 1147–1154.

Aman A, Piotrowski T (2010). Cell migration during morphogenesis. Dev Biol 341, 20–33.

Anon E, Serra-Picamal X, Hersen P, Gauthier NC, Sheetz MP, Trepat X, Ladoux B (2012). Cell crawling mediates collective cell migration to close undamaged epithelial gaps. Proc Natl Acad Sci USA 109, 10891–10896.

Arwert EN, Hoste E, Watt FM (2012). Epithelial stem cells, wound healing and cancer. Nat Rev Cancer 12, 170–180.

Block ER, Matela AR, SundarRaj N, Iszkula ER, Klarlund JK (2004). Wounding induces motility in sheets of corneal epithelial cells through loss of spatial constraints: role of heparin-binding epidermal growth factor-like growth factor signaling. J Biol Chem 279, 24307–24312.

Boulter E, Estrach S, Errante A, Pons C, Cailleteau L, Tissot F, Meneguzzi G, Féral CC (2013). CD98hc (SLC3A2) regulation of skin homeostasis wanes with age. J Exp Med 210, 173–190.
Carnell LS, Siochi EJ, Holloway NM, Stephens RM, Rhim C, Niklason LE, Clark RL (2008). Aligned mats from electrospun single fibers. Macromolecules 41, 5345–5349.
Cavani A, Zambruno G, Marconi A, Manca V, Marchetti M, Giannetti A (1993). Distinctive integrin expression in the newly forming epidermis during wound healing in humans. J Invest Dermatol 101, 600–604.
Chancellor TJ, Lee J, Thodeti CK, Lele T (2010). Actomyosin tension exerted on the nucleus through nesprin-1 connections influences endothelial cell adhesion, migration, and cyclic strain-induced reorientation. Biophys J 99, 115–123.
Clark RAF, Lanigan JM, DellaPelle P, Manseau E, Dvorak HF, Colvin RB (1982). Fibronectin and fibrin provide a provisional matrix for epidermal cell migration during wound reepithelialization. J Invest Dermatol 79, 264–269.
Condeelis J, Segall JE (2003). Intravital imaging of cell movement in tumours. Nat Rev Cancer 3, 921–930.
Deisboeck TS, Couzin ID (2009). Collective behavior in cancer cell populations. Bioessays 31, 190–197.
Demidova-Rice TN, Hamblin MR, Herman IM (2012). Acute and impaired wound healing: pathophysiology and current methods for drug delivery, part 1: normal and chronic wounds: biology, causes, and approaches to care. Adv Skin Wound Care 25, 304–314.
Eming SA, Martin P, Tomic-Canic M (2014). Wound repair and regeneration: mechanisms, signaling, and translation. Sci Transl Med 6, 265sr6.
Faust U, Hampe N, Rubner W, Kirchgessner N, Safran S, Hoffmann B, Merkel R (2011). Cyclic stress at mHz frequencies aligns fibroblasts in direction of zero strain. PLoS One 6, e28963.
Fenteany G, Janmey PA, Stossel TP (2000). Signaling pathways and cell mechanics involved in wound closure by epithelial cell sheets. Curr Biol 10, 831–838.
Friedl P, Gilmour D (2009). Collective cell migration in morphogenesis, regeneration and cancer. Nat Rev Mol Cell Biol 10, 445–457.
Friedl P, Locker J, Sahai E, Segall JE (2012a). Classifying collective cancer cell invasion. Nat Cell Biol 14, 777–783.
Friedl P, Sahai E, Weiss S, Yamada KM (2012b). New dimensions in cell migration. Nat Rev Mol Cell Biol 13, 743–747.
Frykberg RG, Banks J (2015). Challenges in the treatment of chronic wounds. Adv Wound Care 4, 560–582.
Gerhardt H, Golding M, Fruttiger M, Ruhrberg C, Lundkvist A, Abramsson A, Jeltsch M, Mitchell C, Alitalo K, Shima D, Betsholtz C (2003). VEGF guides angiogenic sprouting utilizing endothelial tip cell filopodia. J Cell Biol 161, 1163–1177.
Haeger A, Wolf K, Zegers MM, Friedl P (2015). Collective cell migration: guidance principles and hierarchies. Trends Cell Biol 25, 556–566.
Harding KG, Morris HL, Patel GK (2002). Science, medicine, and the future: healing chronic wounds. BMJ 324, 160–163.
Hielscher AC, Qiu C, Gerecht S (2012). Breast cancer cell-derived matrix supports vascular morphogenesis. Am J Physiol Cell Physiol 302, C1243–C1256.
Hulkower KI, Herber RL (2011). Cell migration and invasion assays as tools for drug discovery. Pharmaceutics 3, 107–124.
Ilina O, Friedl P (2009). Mechanisms of collective cell migration at a glance. J Cell Sci 122, 3203–3208.
Jacinto A, Martinez-Arias A, Martin P (2001). Mechanisms of epithelial fusion and repair. Nat Cell Biol 3, E117–E123.
Keely P, Nain A (2015). Capturing relevant extracellular matrices for investigating cell migration. F1000Research 4.
Kim D-H., Provenzano PP, Smith CL, Levchenko A (2012). Matrix nanotopography as a regulator of cell function. J Cell Biol 197, 351–360.
Klepeis VE, Cornell-Bell A, Trinkaus-Randall V (2001). Growth factors but not gap junctions play a role in injury-induced $Ca^{2+}$ waves in epithelial cells. J Cell Sci 114, 4185–4195.
Krawczyk WS (1971). A pattern of epidermal cell migration during wound healing. J Cell Biol 49, 247–263.
Liang CC, Park AY, Guan JL (2007). In vitro scratch assay: a convenient and inexpensive method for analysis of cell migration in vitro. Nat Protoc 2, 329–333.
Liu Y, Zhang X, Xia Y, Yang H (2010). Magnetic-field-assisted electrospinning of aligned straight and wavy polymeric nanofibers. Adv Mater 22, 2454–2457.
Lovett DB, Shekhar N, Nickerson JA, Roux KJ, Lele TP (2013). Modulation of nuclear shape by substrate rigidity. Cell Mol Bioeng 6, 230–238.
Lutolf MP, Hubbell JA (2005). Synthetic biomaterials as instructive extracellular microenvironments for morphogenesis in tissue engineering. Nat Biotechnol 23, 47–55.
Martin P (1997). Wound healing—aiming for perfect skin regeneration. Science 276, 75–81.
Martin P, Lewis J (1992). Actin cables and epidermal movement in embryonic wound healing. Nature 360, 179–183.
Mayor R, Etienne-Manneville S (2016). The front and rear of collective cell migration. Nat Rev Mol Cell Biol 17, 97–109.
McMahon A, Supatto W, Fraser SE, Stathopoulos A (2008). Dynamic analyses of *Drosophila* gastrulation provide insights into collective cell migration. Science 322, 1546–1550.
Meehan S, Nain AS (2014). Role of suspended fiber structural stiffness and curvature on single-cell migration, nucleus shape, and focal-adhesion-cluster length. Biophys J 107, 2604–2611.
Mustoe T (2004). Understanding chronic wounds: a unifying hypothesis on their pathogenesis and implications for therapy. Am J Surg 187, 65–70.
Nain AS, Wang J (2013). Polymeric nanofibers: isodiametric design space and methodology for depositing aligned nanofiber arrays in single and multiple layers. Polym J 45, 695–700.
Oskeritzian CA (2012). Mast cells and wound healing. Adv Wound Care 1, 23–28.
Patsialou A, Bravo-Cordero JJ, Wang Y, Entenberg D, Liu H, Clarke M, Condeelis JS (2013). Intravital multiphoton imaging reveals multicellular streaming as a crucial component of in vivo cell migration in human breast tumors. IntraVital 2, e25294.
Pittet MJ, Weissleder R (2011). Intravital imaging. Cell 147, 983–991.
Provenzano PP, Inman DR, Eliceiri KW, Knittel JG, Yan L, Rueden CT, White JG, Keely PJ (2008). Collagen density promotes mammary tumor initiation and progression. BMC Med 6, 11.
Provenzano PP, Vanderby R (2006). Collagen fibril morphology and organization: implications for force transmission in ligament and tendon. Matrix Biol 25, 71–84.
Rørth P (2009). Collective cell migration. Annu Rev Cell Dev Biol 25, 407–429.
Rybinski B, Franco-Barraza J, Cukierman E (2014). The wound healing, chronic fibrosis, and cancer progression triad. Physiol Genomics 46, 223–244.
Schäfer M, Werner S (2008). Cancer as an overhealing wound: an old hypothesis revisited. Nat Rev Mol Cell Biol 9, 628–638.
Schaue D, McBride WH (2015). Opportunities and challenges of radiotherapy for treating cancer. Nat Rev Clin Oncol 12, 527–540.
Schedin P, Keely PJ (2011). Mammary gland ECM remodeling, stiffness, and mechanosignaling in normal development and tumor progression. Cold Spring Harb Perspect Biol 3, a003228.
Schmidt M, Paes K, De Mazière A, Smyczek T, Yang S, Gray A, French D, Kasman I, Klumperman J, Rice DS, Ye W (2007). EGFL7 regulates the collective migration of endothelial cells by restricting their spatial distribution. Development 134, 2913–2923.
Sharma P, Sheets K, Elankumaran S, Nain AS (2013). The mechanistic influence of aligned nanofibers on cell shape, migration and blebbing dynamics of glioma cells. Integr Biol (Camb) 5, 1036–1044.
Sheets K, Wang J, Zhao W, Kapania R, Nain AS (2016). Nanonet force microscopy for measuring cell forces. Biophys J 111, 197–207.
Silver FH (2006). Mechanosensing and Mechanochemical Transduction in Extracellular Matrix: Biological, Chemical, Engineering, and Physiological Aspects, Springer Science and Business Media.
Silver FH, Freeman JW, Seehra GP (2003). Collagen self-assembly and the development of tendon mechanical properties. J Biomech 36, 1529–1553.
Somogyi K, Rørth P (2004). Evidence for tension-based regulation of *Drosophila* MAL and SRF during invasive cell migration. Dev Cell 7, 85–93.
Suprynowicz FA, Upadhyay G, Krawczyk E, Kramer SC, Hebert JD, Liu X, Yuan H, Cheluvaraju C, Clapp PW, Boucher RC Jr, *et al.* (2012). Conditionally reprogrammed cells represent a stem-like state of adult epithelial cells. Proc Natl Acad Sci USA 109, 20035–20040.
Tinevez J-Y., Schulze U, Salbreux G, Roensch J, Joanny J-F, Paluch E (2009). Role of cortical tension in bleb growth. Proc Natl Acad Sci USA 106, 18581–18586.
Tsang MW, Wong WK, Hung CS, Lai KM, Tang W, Cheung EY, Kam G, Leung L, Chan CW, Chu CM, Lam EK (2003). Human epidermal growth factor enhances healing of diabetic foot ulcers. Diabetes Care 26, 1856–1861.

Vedula SRK, Hirata H, Nai MH, Brugués A, Toyama Y, Trepat X, Lim CT, Ladoux B (2014). Epithelial bridges maintain tissue integrity during collective cell migration. Nat Mater 13, 87–96.
Vedula SRK, Ravasio A, Lim CT, Ladoux B (2013). Collective cell migration: a mechanistic perspective. Physiology (Bethesda) 28, 370–379.
Versaevel M, Grevesse T, Gabriele S (2012). Spatial coordination between cell and nuclear shape within micropatterned endothelial cells. Nat Commun 3, 671.
Wang W, Wyckoff JB, Frohlich VC, Oleynikov Y, Hüttelmaier S, Zavadil J, Cermak L, Bottinger EP, Singer RH, White JG, *et al*. (2002). Single cell behavior in metastatic primary mammary tumors correlated with gene expression patterns revealed by molecular profiling. Cancer Res 62, 6278–6288.
Wang Y, Gutierrez-Herrera E, Ortega-Martinez A, Anderson RR, Franco W (2016). UV fluorescence excitation imaging of healing of wounds in skin: evaluation of wound closure in organ culture model. Lasers Surg Med 48, 678–685.
Wang J, Nain AS (2014). Suspended micro/nanofiber hierarchical biological scaffolds fabricated using non-electrospinning STEP technique. Langmuir 30, 13641–13649.
Webster MT, Manor U, Lippincott-Schwartz J, Fan CM (2016). Intravital imaging reveals ghost fibers as architectural units guiding myogenic progenitors during regeneration. Cell Stem Cell 18, 243–252.
Weigelin B, Bakker G-J, Friedl P (2014). Intravital third harmonic generation microscopy of collective melanoma cell invasion. IntraVital 1, 32–43.
Weiss P, Matoltsy AG (1959). Wound healing in chick embryos in vivo and in vitro. Dev Biol 1, 302–326.
Wenger MPE, Bozec L, Horton MA, Mesquida P (2007). Mechanical properties of collagen fibrils. Biophys J 93, 1255–1263.
Wirtz D, Konstantopoulos K, Searson PC (2011). The physics of cancer: the role of physical interactions and mechanical forces in metastasis. Nat Rev Cancer 11, 512–522.
Wyld L, Audisio RA, Poston GJ (2015). The evolution of cancer surgery and future perspectives. Nat Rev Clin Oncol 12, 115–124.
Xie J, Macewan ḰMR, Ray ḰWZ, Liu W, Siewe DY, Xia Y (2010). Radially aligned, electrospun nanofibers and tissue regeneration applications. ACS Nano 4, 5027–5036.
Yamaguchi H, Wyckoff J, Condeelis J (2005). Cell migration in tumors. Curr Opin Cell Biol. 17, 559–564.
Yan C, Grimm WA, Garner WL, Qin L, Travis T, Tan N, Han Y-P (2010). Epithelial to mesenchymal transition in human skin wound healing is induced by tumor necrosis factor-alpha through bone morphogenic protein-2. Am J Pathol 176, 2247–2258.
Zelenka PS, Arpitha P (2008). Coordinating cell proliferation and migration in the lens and cornea. Semin Cell Dev Biol 19, 113–124.